RSC Advances

PAPER

View Article Online
View Journal | View Issue

Cite this: *RSC Adv.*, 2024, **14**, 8135

Enhancing OLED emitter efficiency through increased rigidity†

Mahendra Godi, Hyukmin Kwon, Sangwook Park, Sunwoo Park, Hayoon Lee, Kiho Lee and Jongwook Park *

Received 20th November 2023
Accepted 4th March 2024

DOI: 10.1039/d3ra07937f

rsc.li/rsc-advances

Three new blue materials, **TPI-InCz**, **PAI-InCz**, and **CN-PAI-InCz**, have been developed. In the film state, **TPI-InCz** and **PAI-InCz** exhibited emission peaks at 411 and 431 nm indicating deep blue emission. **CN-PAI-InCz** showed a peak emission at 452 nm, within the real blue region. When these three materials were used as the emissive layer to fabricate non-doped devices, **CN-PAI-InCz** showed the highest current efficiency of 2.91 cd A^{-1}, power efficiency of 1.93 lm W^{-1}, and external quantum efficiency of 3.31%. Among the synthesized materials, **CN-PAI-InCz** exhibited superior charge balance due to the introduction of CN groups, as confirmed by hole-only devices and electron-only devices. **PAI-InCz** demonstrated fast hole mobility with a value of 1.50 × 10^{-3} cm^2 V^{-1} s^{-1}, attributed to its planar and highly rigid structure. In the resulting devices, the Commission Internationale de l'Eclairage coordinates for **TPI-InCz**, **PAI-InCz**, and **CN-PAI-InCz** were (0.162, 0.048), (0.0161, 0.067), and (0.155, 0.099), all indicating emission in the blue region.

Introduction

Since the initial development of organic light emitting diodes (OLEDs), there has been a continuous effort to enhance their efficiency through the development of new materials and component technologies. Fluorescent materials have evolved from first-generation chromophores like anthracene, pyrene, and perylene to more recent innovations such as thermally activated delayed fluorescence (TADF) and hyperfluorescence (HF) materials.[1,2] These molecular design strategies share common principles. Firstly, maintaining rigidity and planarity in the molecular structure reduces non-radiative pathways, enhances the oscillator strength, and improves the photoluminescence quantum yield (PLQY). Based on these principles, a chromophore can be extended by using the same chromophore or by fusing different chromophores. For instance, the use of two carbazole moieties, positioned at *ortho*, *meta*, and *para* positions with respect to nitrogen, can extend the chromophore.[3] Well-known examples of this approach include indolocarbazole. Donors of different chromophores, such as benzofurocarbazole and benzothienocarbazole, which are obtained by fusing carbazole with benzofuran or benzothiophene, have also been developed.[4–6] Recently, materials with improved rigidity, based on the *v*-DABNA backbone and known as HF materials, have been reported.[7,8] The second key principle involves conferring bipolar characteristics to maintain charge balance. Polycyclic aromatic hydrocarbon materials commonly exhibit superior hole characteristics, demonstrating fast hole mobility but inferior electron characteristics. Consequently, when applied in OLED components, they can experience significant roll-off at high current densities.[9,10] Charge injection and transport in OLED layers are important factors in enhancing electroluminescence (EL) performance, necessitating the advantageous bipolar characteristics for both electron and hole transport. Typically, introducing electron donor such as carbazole, dibenzofuran, and dibenzothiophene, along with electron acceptor like diphenylamine, triphenylamine, and triazine, allows for the straightforward development of bipolar materials.[11–13] However, high planarity may induce molecular packing, leading to aggregation-caused quenching phenomena, potentially diminishing efficiency.[14] Moreover, the combination of donors and acceptors with strong abilities to impart bipolar characteristics, often results in significant charge transfer (CT), which poses challenges in achieving blue emission.[15]

In this study, among several indolocarbazoles, indolo[2,3-*b*]carbazole (InCz) was chosen as the electron donor, and three electron-accepting groups, namely, triphenyl-imidazole (TPI), phenanthrol-imidazole (PAI), and CN-substituted PAI (CN-PAI), were combined to design and synthesize three materials: 3,9-di-*tert*-butyl-5,7-bis(4-(1,4,5-triphenyl-1*H*-imidazol-2-yl)phenyl)-5,7-dihydroindolo[2,3-*b*]carbazole (**TPI-InCz**), 3,9-di-*tert*-butyl-5,7-bis(4-(1-phenyl-1*H*-phenanthro[9,10-*d*]imidazol-2-yl) phenyl)-5,7-dihydroindolo[2,3-*b*]carbazole (**PAI-InCz**), and 4,4′-(((3,9-di-*tert*-butylindolo[2,3-*b*]carbazole-5,7-diyl)bis(4,1-phenylene))bis(1*H*-phenanthro[9,10-*d*]imidazole-2,1-diyl))

Integrated Engineering, Department of Chemical Engineering, Kyung Hee University, Gyeonggi 17104, Republic of Korea. E-mail: jongpark@khu.ac.kr

† Electronic supplementary information (ESI) available. CCDC 2302318. For ESI and crystallographic data in CIF or other electronic format see DOI: https://doi.org/10.1039/d3ra07937f

dibenzonitrile (**CN-PAI-InCz**). InCz exhibits superior hole characteristics compared to carbazole and possesses high rigidity.[16] Furthermore, it can be utilized as either a host or dopant depending on the substituent moiety, offering versatility. L. Duan group developed a green host, 23blCTRZ, using InCz and triphenyl-triazine, achieving an external quantum efficiency (EQE) of 19.2%. The combination of these two moieties, connected at the *meta* position in m23blCTRZ, was used as a TADF sensitizer.[17,18] Q. Zhang *et al.* synthesized TADF green dopants, BBCz-*o*-TRZ, and BBCz-*o*-2TRZ by combining InCz with triphenyl-triazine at the *ortho* position, showing EQEs of 16.5% and 17.5%.[19] In the study by J. Y. Lee's group, electron-accepting CN groups were introduced to 23blCTRZ, enhancing the electron-accepting ability to create TADF green dopant ICBNTrz1, achieving an EQE of 14.8%.[20] While many studies have utilized InCz and triazine derivatives to develop emitting materials, strong CT occurring within the molecules has resulted in green emission. However, in this study, the use of TPI, PAI, and CN-PAI as weak electron acceptors, when combined with InCz, maintains bipolar characteristics, allowing for blue emission. Additionally, their high planarity, when combined with InCz, raises expectations for a high PLQY and improved device efficiency. The photophysical, thermal, and electroluminescence properties of the synthesized **TPI-InCz**, **PAI-InCz**, and **CN-PAI-InCz** are investigated, and theoretical calculation results are presented.

Experimental

Synthesis of 1,5-dibromo-2,4-dinitrobenzene (1)

1,3-Dibromobenzene (7.0 g, 29.7 mmol) was slowly added to a stirring mixture of concentrated sulfuric acid (6.5 mL) and fuming nitric acid (6.5 mL) while being cooled in an ice bath at 10–20 °C. After the addition was complete, the temperature was raised to 50 °C and maintained for 30–40 minutes. The reaction mixture was then poured onto crushed ice. The solid precipitate formed was collected by filtration and washed several times with chilled water. The solid was then dissolved in a mixture of ethanol (90 mL) and acetone (20 mL). The solution was filtered and cooled in the fridge until a precipitate formed. The crystals collected were washed with cold ethanol to obtain 1,5-dibromo-2,4-dinitrobenzene (6.73 g, 20.7 mmol) as a bright yellow solid with a yield of 70%.

^{1}H NMR (400 MHz, $CDCl_3$) δ (ppm) 8.45 (1H, $J = 6.25$ Hz, s), 8.22 (1H, s). ^{13}C NMR (100 MHz, $CDCl_3$) δ (ppm) 148.2, 141.50, 123.00, 120.00.

Synthesis of 2-(4-(*tert*-butyl) phenyl)-4,4,5,5-tetramethyl-1,3,2-dioxaborolane (2)

In an oven-dried Schlenk flask under an argon atmosphere, 1-bromo-4-(*tert*-butyl)benzene (4.90 mL, 28.2 mmol) and 8.58 g of bis(pinacolato)diboron (33.8 mmol) were dissolved in 60 mL of toluene. Oven-dried potassium acetate (4.14 g, 42.2 mmol) was quickly added to the mixture, followed by [1,1′-bis(diphenylphosphino)ferrocene]palladium(II) dichloride ($Pd(dppf)Cl_2$) (0.548 g, 1.13 mmol). The mixture was heated at 90 °C overnight. The mixture was then cooled to room temperature, and 100 mL of ethyl acetate (EA) was added to quench the reaction. DI water (30 mL) was added to extract the aqueous phase, and 50 mL of brine (2×) was used to wash the organic phase. It was then dried over anhydrous $MgSO_4$ and filtered. After concentrating down the filtrate, silica column chromatography with hexanes as the eluent gave 5.57 g of white powder (76%). ^{1}H NMR (400 MHz, $CDCl_3$) δ (ppm) 7.82–7.81 (d, 2H), 7.45–7.43 (d, $J = 8.0$ Hz, 2H), 1.36–1.37 (s, 21H). ^{13}C NMR (100 MHz, $CDCl_3$) δ (ppm): 154.42, 134.67, 124.65, 83.53, 34.83, 31.15, 24.79.

Synthesis of 4,4″-di-*tert*-butyl-4′,6′-dinitro-1,1′:3′,1″-terphenyl (3)

Compound (**1**) (5 g, 1.5 mmol), compound (**2**) (1.03 g, 3.3 mmol), a 2 M aqueous potassium carbonate (K_2CO_3) solution (10 mL, 8.0 mmol), and tetrakis(triphenylphosphine)-palladium(0) ($Pd(PPh_3)_4$) (0.085 g, 0.007 mmol) in toluene (30 mL) were stirred at 100 °C for 24 hours. After cooling to room temperature, the reaction was quenched with water. The resulting mixture was extracted with EA and dried over anhydrous $MgSO_4$. The solvent was removed, and the residue was purified through column chromatography using an eluent (EA : hexane = 0.5 : 9.5) to yield a yellow residue in 83%. ^{1}H NMR (400 MHz, $CDCl_3$) δ (ppm) 8.38 (1H, s), 7.55 (1H, s), 7.48–7.44 (4H, d), 7.29–7.26 (4H, $J = 8.0$ Hz d), 1.34 (18H, s). ^{13}C NMR (100 MHz, $CDCl_3$) δ (ppm) 152.73, 147.18, 140.18, 135.97, 132.46, 127.64, 126.09, 120.80, 34.87, 31.31.

Synthesis of 3,9-di-*tert*-butyl-5,7-dihydroindolo[2,3-*b*]carbazole (InCz) (4)

Compound (**3**) (5.0 g, 0.68 mmol), triethylphosphite (11.5 g, 6 eq.), and 1,2-dichlorobenzene 1 mL was stirred at 180 °C for 2 days. Under nitrogen atmosphere. The reaction mixture was allowed to cool to room temperature. Then solvent was removed *in vacuo*, then the crude product was purified by recrystallization from ethanol to yielding the title compound (1.35 g, 32%) as white solid. ^{1}H NMR (DMSO, 400 MHz) δ (ppm) 10.85 (s, 2H), 8.62 (s, 4 $J = 1.5$ Hz, 1H), 7.98–8.01 (d, 2H), 7.35 (d, 4 $J = 1.5$ Hz, 2H), 7.29 (s, 1H), 7.16–7.19 (d, 2H) 1.35 (s, 18H). ^{13}C NMR (100 MHz, DMSO) δ (ppm) 147.77, 141.06, 140.65, 121.38, 119.30, 117.55, 116.48, 111.07,107.14, 91.22, 35.22, 32.24. HRMS (FAB-MS, *m*/*z*): calcd for $C_{34}H_{44}N_2$, 368.2; found: 368.22 $[M]^+$.

Synthesis of 2-(4-bromophenyl)-1,4,5-triphenyl-1*H*-imidazole (TPI-Br) (5)

A mixture of benzil (2.10 g, 10.0 mmol), 4-bromobenzaldehyde (1.85 g, 10.0 mmol), aniline (3.65 mL, 40.0 mmol), ammonium acetate (3.85 g, 50.0 mmol), and acetic acid (50 mL) was refluxed under nitrogen at 120 °C in an oil bath for 2 hours. After the mixture was cooled down and filtered, the solid product was washed with a 50 mL mixture of acetic acid and water (1 : 1) and 50 mL of water. It was then dissolved in methylene chloride (MC) and dried with anhydrous sodium sulfate (Na_2SO_4). The product was subsequently purified by silica gel chromatography using a mixture of MC and petroleum ether as the eluent,

resulting in the isolation of a pure, dry white product (3.83 g, yield: 85%). ^{1}H NMR (400 MHz, $CDCl_3$) δ (ppm) 7.61–7.59 (d, 2H), 7.38–7.36 (d, J = 8 Hz, 3H), 7.28–7.19 (m, 11H), 7.19–7.13 (m, 2H), 7.05–7.03 (m, 2H). ^{13}C NMR (100 MHz, $CDCl_3$) δ (ppm) 145.87, 138.61, 136.98, 134.36, 131.43, 131.33, 131.18, 130.50, 130.45, 129.57, 129.38, 128.64, 128.52, 128.47, 128.34, 128.21, 127.48, 126.86, 122.76.

Synthesis of 2-(4-bromophenyl)-1-phenyl-1*H*-phenanthro [9,10-*d*]imidazole (PAI-Br) (6)

A mixture of 9,10-phenanthrenequinone (4.16 g, 20 mmol), aniline (7.4 mL, 80 mmol), 4-bromobenzaldehyde (3.70 g, 20 mmol), ammonium acetate (7.7 g, 100 mmol), and acetic acid (50 mL) was heated to 120 °C and stirred for 2 hours under a nitrogen atmosphere. After cooling to room temperature, the mixture was filtered to yield a yellow solid, which was washed with a small amount of acetic acid and water, and then dried under vacuum. The crude products were purified by column chromatography with MC to obtain a white solid (7.71 g, yield = 86%). The products were not further purified and were directly used for the next reaction. ^{1}H NMR (400 MHz, $CDCl_3$) δ (ppm) 8.86–8.84 (dd, 1H), 8.75–8.73 (dd, 1H), 8.69–8.67 (dd, 1H), 7.76–7.72 (t, 1H), 7.64–7.59 (m, 4H), 7.48–7.42 (m, 7H), 7.26–7.23 (dd, 1H), 7.16–7.14 (d, 1H). ^{13}C NMR (100 MHz, $CDCl_3$) δ (ppm) 149.81, 138.62, 137.52, 131.54, 130.89, 130.40, 130.09, 129.55, 129.44, 129.11, 128.40, 127.45, 127.20, 126.43, 125.84, 125.14, 124.23, 123.45, 123.25, 123.01, 122.77, 120.93.

Synthesis of 4-(2-(4-bromophenyl-1*H*-phenanthro(9,10-*d*) imidazol-1-yl)) benzonitrile (CN-PAI-Br) (7)

A mixture of 4-bromobenzaldehyde (0.92 g, 5.0 mmol) and phenanthrenequinone (1.04 g, 5.0 mmol), 4-aminobenzonitrile (2.36 g, 20 mmol) and ammonium acetate (1.85 g, 25 mmol), along with 15 mL of acetic acid, was added to a clean 100 mL round bottom flask. The mixture was refluxed under a nitrogen atmosphere at 120 °C in an oil bath for 2 hours. After cooling, the solid product was filtered and washed with 30 mL of a 1 : 1 water/acetic acid solution, followed by rinsing with 30 mL of water. It was dissolved in $CHCl_3$ and dried with $MgSO_4$ overnight. The product was purified by column chromatography, and 2.08 g (4.4 mmol) of white product was obtained, with a yield of 88%. ^{1}H NMR (400 MHz, DMSO) δ (ppm) 8.92–8.90 (d, 1H), 8.86–8.84 (d, 1H), 8.65–8.63 (d, 1H), 8.17–8.14 (d, 2H), 7.97–7.94 (d, 2H), 7.76–7.73 (t, 1H), 7.68–7.65 (t, 1H), 7.57–7.53 (t, 3H), 7.42–7.35 (m, 3H), 7.03 (d, H). ^{13}C NMR (100 MHz, DMSO) δ (ppm) 150.02, 142.53, 137.26, 135.07, 131.95, 131.78, 131.05, 129.59, 129.15, 128.31, 128.24, 128.17, 127.56, 127.01, 126.58, 126.08, 125.20, 124.28, 123.48, 122.61, 122.58, 120.78, 118.65, 113.66.

Synthesis of 3,9-di-*tert*-butyl-5,7-bis(4-(1,4,5-triphenyl-1*H*-imidazol-2-yl) phenyl)-5,7-dihydroindolo [2,3-*b*]carbazole (TPI-InCz)

Under a nitrogen atmosphere, compound (**4**) (0.35 g, 1.0 mmol), compound (**5**) (0.90 g, 2.1 mmol), tris(dibenzylideneacetone) dipalladium(0) ($Pd_2(dba)_3$ (0.05 g, 0.06 mmol), and 20.0 mL of toluene were added to a 50 mL Schlenk flask. After stirring for 20 minutes at room temperature, sodium *tert*-butoxide (*t*-BuONa) (0.27 g, 3.0 mmol) and tri-*tert*-butylphosphine (P(*t*-Bu)$_3$) (10% in toluene, 0.1 mmol) were sequentially added, and the mixture was stirred at 90 °C for 5 hours. After the reaction was complete, the solvent was removed, and the residue was purified by silica gel column chromatography using an eluent tetrahydrofuran (THF) : hexane = 3 : 7) to yield (7.50 g, 71% yield) a white solid. ^{1}H NMR (400 MHz, THF) δ (ppm) 8.76 (s, 1H), 8.11–8.09 (d, 2H), 7.70–7.67 (d, 4H), 7.64–7.61 (m, 4H), 7.55–7.52 (m, 4H), 7.40–7.32 (m, 11H), 7.24–7.17 (m, 1 4H), 7.16–7.07 (m, 6H), 1.35 (s, 18H). ^{13}C NMR (100 MHz, $CDCl_3$) δ (ppm) 148.89, 146.32, 141.43, 140.87, 138.61, 138.02, 137.08, 134.50, 131.27, 131.24, 130.66, 130.49, 129.18, 128.72, 128.57, 128.31, 128.27, 127.51, 126.41, 121.78, 119.19, 118.91, 118.10, 111.05, 106.02, 89.29, 35.29, 31.90 ppm. HRMS (FAB-MS, m/z): calcd for $C_{80}H_{64}N_6$, 1105.49; found: 1105.49 $[M]^+$.

Synthesis of 3,9-di-*tert*-butyl-5,7-bis(4-(1-phenyl-1*H*-phenanthro[9,10-*d*]imidazol-2-yl) phenyl)-5,7-dihydroindolo [2,3-*b*]carbazole (PAI-InCz)

Under a nitrogen atmosphere, compound (**4**) (0.35 g, 1.0 mmol), compound (**6**) (0.91 g, 2.1 mmol), $Pd_2(dba)_3$ (0.05 g, 0.06 mmol), and 20.0 mL of toluene were added to a 50 mL Schlenk flask. After stirring for 20 minutes at room temperature, *t*-BuONa (0.27 g, 3.0 mmol) and P(*t*-Bu)$_3$ (10% in toluene, 0.1 mmol) were sequentially added, and the mixture was stirred at 90 °C for 5 hours. After the reaction was completed, the solvent was removed, and the residue was purified by silica gel column chromatography using an eluent of THF : hexane = 3 : 7 to yield 750 mg (71% yield) of a white solid. ^{1}H NMR (400 MHz, THF) δ (ppm) 8.88–8.86 (dd, 2H), 8.83–8.81 (dd, 2H), 8.78–8.74 (m, 3H), 8.13–8.11 (d, 2H), 7.92–7.90 (m, 4H), 7.89–7.71 (m, 10H), 7.67–7.57 (m, 8H), 7.48–7.34 (m, 17H), 7.28–7.18 (m, 4H), 1.37 (s, 18H). ^{13}C NMR (100 MHz, $CDCl_3$) δ (ppm) 150.20, 148.98, 141.40, 140.82, 138.70, 138.58, 137.65, 130.99, 130.48, 130.23, 129.44, 129.22, 128.44, 128.38, 127.47, 127.31, 126.51, 125.80, 125.13, 124.22, 123.26, 123.10, 122.85, 121.82, 121.05, 119.22, 119.0, 106.05, 35.31, 31.91, 30.42. HRMS (FAB-MS, m/z): calcd for $C_{80}H_{60}N_6$, 1109.52; found: 1109.52 $[M]^+$.

Synthesis of 4,4′-(((3,9-di-*tert*-butylindolo[2,3-*b*]carbazole-5,7-diyl) bis(4,1-phenylene))bis(1*H*-phenanthro[9,10-*d*]imidazole-2,1-diyl))dibenzonitrile (CN-PAI-InCz)

Under a nitrogen atmosphere, compound (**4**) (0.35 g, 1.0 mmol), compound (7) (0.95 g, 2.1 mmol), $Pd_2(dba)_3$ (0.05 g, 0.06 mmol), and 20.0 mL of toluene were added to a 50 mL Schlenk flask. After stirring for 20 minutes at room temperature, *t*-BuONa (0.27 g, 3.0 mmol) and P(*t*-Bu)$_3$ (10% in toluene, 0.1 mmol) were sequentially added, and the mixture was stirred at 90 °C for 5 hours. After the reaction was completed, the solvent was removed, and the residue was purified by silica gel column chromatography using an eluent of THF : hexane = 3 : 7 to yield 0.80 g (73% yield) of a yellow solid. ^{1}H NMR (400 MHz, $CDCl_3$) δ (ppm) 8-82-8.79 (m, 4H), 8.73–8.71 (m, 3H), 8.15 (d, 2H), 8.13–8.04 (m, 4H), 7.82–7.80 (m, 3H), 7.77–7.75 (m, 4H), 7.68–7.65

(m, 4H), 7.58–7.54 (m, 6H), 7.41–7.31 (ddt, 2H), 7.34–7.30 (m, 4H), 7.20–7.15 (t, 3H), 1.40 (s, 18H). ^{13}C NMR (100 MHz, $CDCl_3$) δ (ppm) 150.20, 148.98, 141.40, 140.82, 138.70, 138.58, 137.65, 130.99, 130.48, 130.23, 129.44, 129.22, 128.44, 128.38, 127.47, 127.31, 126.51, 125.80, 125.13, 124.22, 123.26, 123.10, 122.85, 121.82, 121.05, 119.22, 119.0, 106.05, 35.31, 31.91, 30.42. HRMS (FAB-MS, m/z): calcd for $C_{82}H_{58}N_8$, 1145.42; found: 1145.48 $[M]^+$ CCDC 2302318.

Results and discussion

Molecular design and synthesis

Fig. 1 shows the chemical structures of the synthesized compounds. These compounds were designed and synthesized as new luminescent materials by using InCz as the electron-donating group and introducing *t*-butyl substitutions to prevent π–π interactions between InCz moieties. InCz is characterized by excellent hole properties and high rigidity. To impart variations in electron-accepting abilities, three electron-accepting groups, TPI, PAI, CN-PAI, were individually incorporated, resulting in three distinct structures for the newly developed materials. While TPI and PAI share similar structures, they differ in rigidity, and CN-PAI exhibits the highest electron-accepting characteristics among the three moieties.

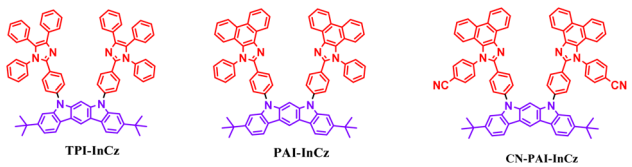

Fig. 1 Chemical structures of newly synthesized materials.

The overall synthetic approach is outlined in Scheme 1, with detailed synthesis procedures provided in the Experimental section. Synthesis involved steps such as bromination, Miyaura borylation, nitration, Suzuki coupling, cyclization, and Buchwald–Hartwig amination. The synthesized materials were purified through column chromatography and recrystallization using silica gel. The chemical structures of the synthesized materials were confirmed through ^{1}H NMR, ^{13}C NMR, and mass spectrometry analysis.

Photophysical properties and theoretical calculation

In Fig. 2 and Table 1, we summarize the optical properties of the synthesized compounds. The absorption spectra of the three synthesized materials were similar. The main absorption occurred around 300–310 nm, corresponding to π–π* transitions by InCz and the imidazole derivatives, and a weak n–π* transition absorption by indolocarbazole around 320–330 nm.[21] In the solution state, the photoluminescence maximum values (PL_{max}) for **TPI-InCz**, **PAI-InCz**, and **CN-PAI-InCz** were 390, 400, and 430 nm, respectively. **PAI-InCz** exhibited red-shifted emission in the longer wavelength range compared to **TPI-InCz** due to extended molecular conjugation, while **CN-PAI-InCz** showed the most significant red-shifted emission due to the introduction of CN groups.[22] Unlike the other two compounds, **PAI-InCz** exhibited two emission peaks at 400 and 417 nm, likely attributed to its high rigidity. This is due to the increased rigidity in **PAI-InCz** resulting from the fused ring, as compared to the structures of **TPI-InCz** and **PAI-InCz**. When comparing the structures of **PAI-InCz** and **CN-PAI-InCz**, the observation can be explained not only by the rotation of the CN group based on a single bond but also by the intramolecular CT between the InCz moiety and CN groups. The full-width at half-maximum

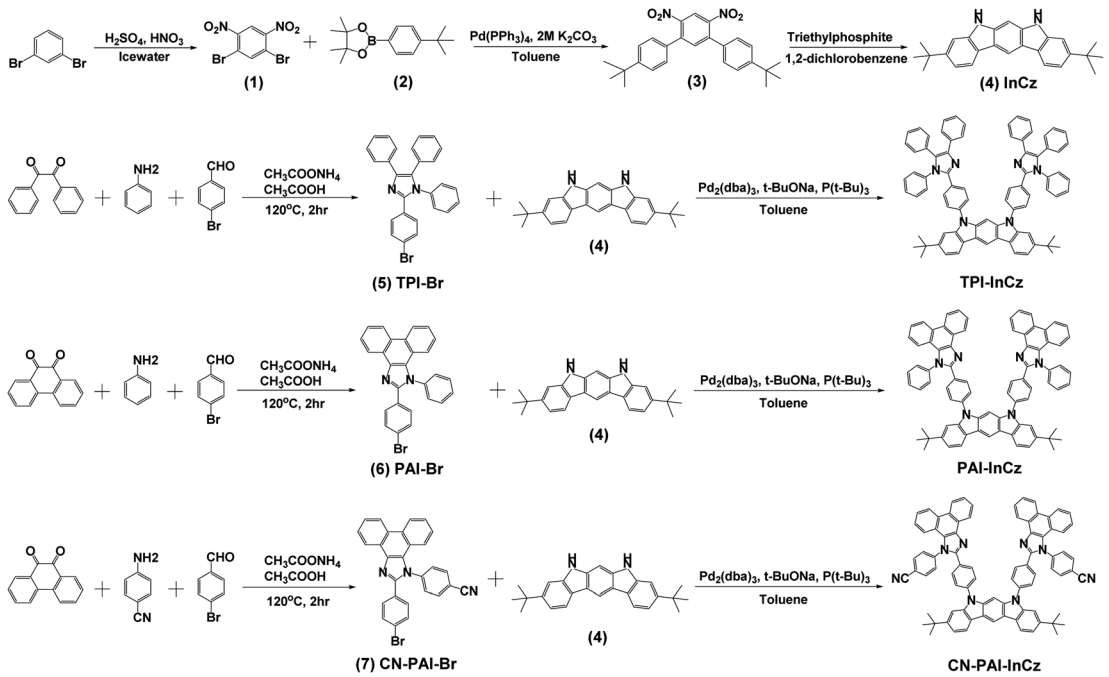

Scheme 1 Synthetic route of TPI-InCz, PAI-InCz and CN-InCz.

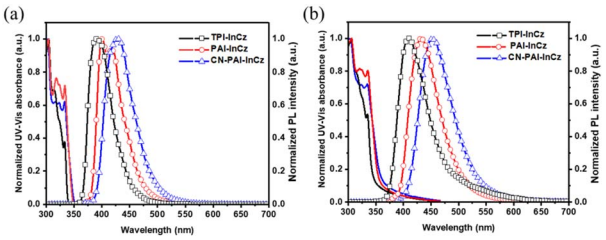

Fig. 2 Optical properties of UV-vis and PL spectra (a) in solution state (concentration: 1×10^{-5} M in toluene), (b) in film state (thickness: 50 nm).

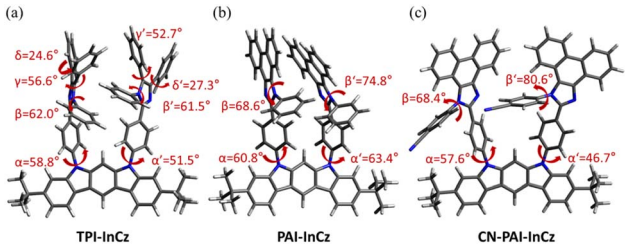

Fig. 3 Optimized structures and dihedral angles calculated with B3LYP-D3/6-31G(d) by ORCA: (a) **TPI-InCz**, (b) **PAI-InCz**, (c) **CN-PAI-InCz**.

(FWHM) values were 48, 51, and 60 nm for **TPI-InCz**, **PAI-InCz**, and **CN-PAI-InCz**, respectively. While **TPI-InCz** and **PAI-InCz** showed similar molecular structures, **CN-PAI-InCz**, with its introduced CN group, exhibited increased intramolecular CT characteristics, leading to a broader emission profile.[23] Typically, in the change from a solution state to a film state, the closer molecular proximity due to intermolecular interactions results in red shifts and broadening of PL_{max} wavelengths. The ultraviolet-visible (UV-vis) spectra shapes of the three synthesized materials in film state showed slightly broader patterns compared to the solution state, with UV-vis maximum peaks (UV_{max}) red-shifted by approximately 2–6 nm. Similarly, the PL max values for **TPI-InCz**, **PAI-InCz**, and **CN-PAI-InCz** were 410, 431, and 452 nm, respectively, representing a red shift of approximately 20–31 nm compared to the solution state. **TPI-InCz** and **CN-PAI-InCz** exhibited relatively smaller red shifts of 20 and 22 nm due to the diphenyl group in TPI and the introduced CN groups preventing strong molecular packing.[24] However, **PAI-InCz**, which possesses the strongest rigid characteristics among the three materials, showed a significant difference of 31 nm between its solution and film states, attributed to strong intermolecular interactions.[25] The FWHM values of PL spectra for **TPI-InCz** and **PAI-InCz** were similar at 60 and 63 nm in the film state, whereas **CN-PAI-InCz** had a larger FWHM of 70 nm. The similar FWHM of **TPI-InCz** and **PAI-InCz** is attributed to the suppressed molecular motion of TPI in the film state. **CN-PAI-InCz** exhibited a broader FWHM compared to that in its solution state, attributed to its closer molecular packing resulting in both intramolecular and intermolecular CT interactions.

To gain a more detailed understanding of the molecular structure, optimized structures were computed using the ORCA computation program with the B3LYP-D3/6-31G(d) level of theory (Fig. 3).[26] The dihedral angles (α and α') between InCz and the introduced TPI, PAI, and CN-PAI were in the range of 47–63°. On the other hand, the dihedral angles of the phenyl groups located on the imidazole moiety, denoted as β and β', exhibited differences, ranging from 62–81°. **TPI-InCz** showed the smallest β and β' angles at 62°, as it experienced steric hindrance from adjacent phenyl groups. However, the neighboring phenyl groups showed twist angles of γ, $\gamma' = 57$, 53° and δ, $\delta' = 25$, 27°, effectively preventing molecular packing. The β and β' angles of **PAI-InCz** and **CN-PAI-InCz** were similar. To further investigate, single crystal X-ray diffraction (XRD) data of **CN-PAI-InCz** was collected for additional confirmation (Fig. 4(a) and S1(a)†). Additional data for single crystals are included in ESI.† Single crystals could not be obtained for **TPI-InCz** and **PAI-InCz**. The dihedral angles between InCz and CN-PAI in **CN-PAI-InCz** were found to be α and $\alpha' = 59.3$, 59.6°, closely matching the computed results. The dihedral angles of phenyl groups on the imidazole moiety were β and $\beta' = 53.6$, 52.7°. In the packing structure, the electron donor InCz and the electron acceptor CN-PAI were found to be parallel, with a distance of approximately 4.5 Å between the two moieties, indicating the possibility of intermolecular CT.[27,28] This observation aligns with the results of the previously confirmed optical properties (Fig. 4(b) and S1(b–d)†).

The electron density distributions in the Highest Occupied Molecular Orbital (HOMO) and Lowest Unoccupied Molecular Orbital (LUMO) were calculated using density functional theory

Table 1 Photophysical properties

	Solution[a]							Film[b]		
	UV_{max} (nm)	PL_{max} (FWHM) (nm)	PLQY (%)	τ_F (ns)	k_r (10^8 s^{-1})	k_{nr} (10^7 s^{-1})	k_r/k_{nr}	UV_{max} (nm)	PL_{max} (FWHM) (nm)	PLQY (%)
TPI-InCz	304 315, 324 333	390(48)	66.4	2.5	2.66	13.4	1.99	306 316, 325 335	410(60)	38.2
PAI-InCz	304 318, 324 333	400 417(51)	87.7	9.3	0.94	1.32	7.12	305 320, 325 335	431(63)	55.3
CN-PAI-InCz	303 316, 323 333	430(60)	68.8	3.9	1.76	8.00	2.20	304 322, 325 335	452(70)	45.1

[a] Concentration: 1×10^{-5} M (in toluene). [b] Evaporated film on glass (thickness: 50 nm).

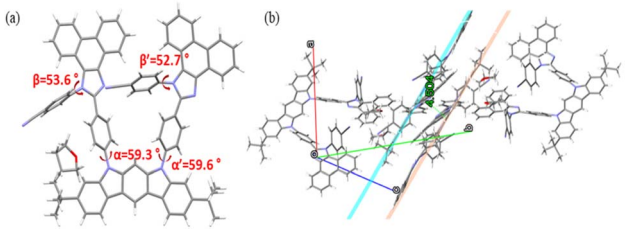

Fig. 4 (a) Single crystal structure of **CN-PAI-InCz** THF, (b) intermolecular packing geometries of **CN-PAI-InCz** THF in the single crystal determined by XRD analysis.

(DFT) (Fig. 5). In the HOMO, it is evident that electron density extends from the electron donor, InCz, to the electron acceptors, TPI, PAI, and CN-PAI. In the LUMO, for **TPI-InCz** and **PAI-InCz**, electron density is observed in the electron acceptors, TPI and PAI. However, for **CN-PAI-InCz**, the LUMO electron density is primarily found on the phenyl group where CN is substituted. In a typical bipolar structure, the electron density in the HOMO resides in the donor, while the electron density in the LUMO is found in the acceptor, with a clear separation between HOMO and LUMO.[29] However, **TPI-InCz** and **PAI-InCz** exhibit significant overlap between HOMO and LUMO due to the weak electron-accepting abilities of TPI and PAI. Therefore, among the three synthesized materials, **CN-PAI-InCz** shows the relatively stronger bipolar properties, while **TPI-InCz** and **PAI-InCz** exhibit relatively weaker bipolar characteristics.

This can be further confirmed through additional solvatochromism experiments. PL spectra were measured in seven different solvents with varying polarities, ranging from toluene to DMSO, each exhibiting different dielectric constants (Table S1 and Fig. S2†). In solvents with low solubility, PL spectra could not be measured. For **TPI-InCz** and **PAI-InCz**, the change in PL_{max} showed a relatively small variation of 22 nm and 18 nm, as the solvent's dielectric constant increased from 2.38 in toluene to 46.7 in DMSO. However, in the case of **CN-PAI-InCz**, the PL_{max} shifted significantly from 430 to 470 nm, representing a 40 nm shift. Additionally, the FWHM of **CN-PAI-InCz** was considerably broadened. This is because as solvent polarity increases, bipolar characteristics stabilize their excited states, resulting in a redshift of the PL wavelength and stronger interactions with the solvent, leading to a broadening of the FWHM.[15,30] Therefore, the most planar **PAI-InCz** exhibited the least significant solvent effect due to strong intermolecular forces, while **CN-PAI-InCz** showed relatively strong bipolar characteristics attributed to the introduced CN group. Such bipolar characteristics can help achieve a good charge balance between holes and electrons in OLED devices, contributing to enhanced EQE. The PLQY of the synthesized three materials were measured in solution and were found to be 66%, 87%, and 68%, respectively. Planar molecular structures generally exhibit high oscillator strengths, resulting in high PLQY values. In the case of **PAI-InCz**, its inclusion of fused rings led to the highest rigidity among the three materials, contributing to its high PLQY value. Time-resolved photoluminescence (TRPL) was used to measure fluorescence lifetime (τ_F), which allowed for the calculation of the radiative rate constant (k_r) and non-radiative rate constant (k_{nr}) (Fig. S3†). The τ_F values for **TPI-InCz**, **PAI-InCz**, and **CN-PAI-InCz** were measured as 2.5, 9.3, and 3.9 ns, respectively. **TPI-InCz** exhibited the lowest PLQY among the three materials due to significant k_{nr} caused by molecular motion of TPI's phenyl groups. Among the three materials, **PAI-InCz** exhibited the highest k_r/k_{nr} ratio. This result is attributed to the utilization of high structural rigidity, effectively reducing non-radiative decay pathways and facilitating the achievement of a high PLQY. In the case of **CN-PAI-InCz**, it is believed that the PLQY decrease was caused by CT characteristics. Therefore, when comparing k_r/k_{nr} values, the order was **TPI-InCz** = 1.99 < **CN-PAI-InCz** = 2.20 < **PAI-InCz** = 7.12. Typically, PLQY decreases in the film state compared to the solution state due to intermolecular packing leading to luminescence quenching. **TPI-InCz**, **PAI-InCz**, and **CN-PAI-InCz** showed a similar tendency, with PLQY values decreasing to 38%, 55%, and 45% in the film state compared to their solution state counterparts. The PL of the synthesized three materials was measured at 77 K, and the calculated triplet energy level (T_1) based on the onset of the spectrum ranged from 2.58 to 2.68 eV, with ΔE_{ST} values exceeding 0.3 eV. Moreover, the absence of delayed fluorescence observed through TRPL suggests that none of the three materials exhibit TADF characteristics (Fig. S4 and Table S2†).

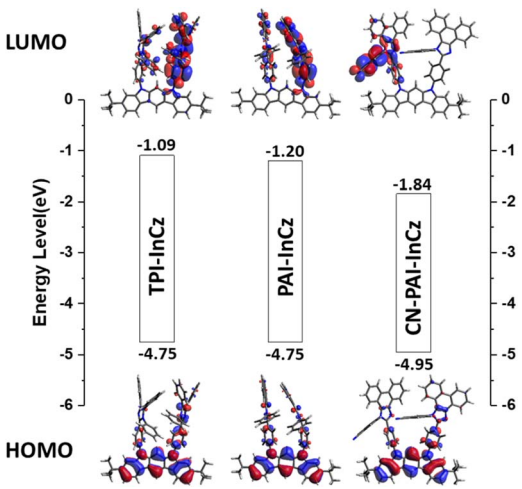

Fig. 5 Electron density distributions and energy levels calculated with B3LYP-D3/6-31G(d) by ORCA.

Electrical and thermal properties

The HOMO values were determined through ultraviolet photoelectron spectra (Riken-Keiki, AC-2), and the optical band gaps were derived by measuring the absorption edges from plots of $(h\nu)$ *versus* $(\alpha h\nu)^2$, where α, h, and ν represent the absorbance, Planck's constant, and the frequency of light, respectively. For **TPI-InCz** and **PAI-InCz**, the HOMO energy levels were similar, with values of −5.49 and −5.47. However, in the case of **CN-PAI-InCz**, the introduction of the CN group resulted in relatively deeper HOMO and LUMO levels of −5.73 and −2.78 due to the withdrawing effect of the CN group.[31] The band gap values were

Table 2 HOMO and LUMO energy levels and band gaps of synthesized materials

	Experimental values			Calculated values by ORCA[d]		
	HOMO[a] (eV)	LUMO[b] (eV)	Band gap[c] (eV)	HOMO (eV)	LUMO (eV)	Band gap (eV)
TPI-InCz	−5.49	−2.53	3.20	−4.75	−1.09	3.66
PAI-InCz	−5.47	−2.45	3.02	−4.75	−1.20	3.55
CN-PAI-InCz	−5.73	−2.78	2.95	−4.95	−1.84	3.11

[a] HOMO value measured by UV photoelectron yield spectroscopy (AC-2). [b] The LUMO value was calculated from the HOMO value and optical bandgap. [c] Optical band gaps were derived by measuring the absorption edges. [d] Calculated at the B3LYP-D3/6-31G(d) level.

affected by the extended conjugation and the CT characteristics occurring within the molecules. **CN-PAI-InCz** exhibited the smallest band gap of 2.95 eV, while **PAI-InCz** and **TPI-InCz** had band gap values of 3.20 and 3.02 eV. The calculated LUMO levels were observed in the order of **TPI-InCz** and **PAI-InCz** with values of −2.53 and −2.45 eV, respectively. The values predicted by molecular calculations for HOMO levels were −4.75, −4.75, and −4.95 eV, and the LUMO levels were −1.09, −1.20, and −1.84 eV for **TPI-InCz**, **PAI-InCz**, and **CN-PAI-InCz**, respectively. The measured and predicted energy levels showed similar trends (Table 2).

To investigate the electrochemical properties of the three compounds, cyclic voltammograms (CV) were measured. All three materials exhibited reversible redox peaks based on electron-donating groups in the range of 0.95 to 1.45 V, as well as reversible redox peaks based on electron-withdrawing groups in the range of −0.95 to −1.5 V. The electrochemical properties remained highly stable even after 50 consecutive scans, with consistent oxidation and reduction currents. This can be considered indirect evidence of the bipolar nature of the molecules (Fig. S5†). Thermogravimetric analysis (TGA) and differential scanning calorimetry (DSC) were conducted to assess the thermal stability and characteristics of the synthesized materials. The obtained data showed that the synthesized materials exhibited very high thermal stability. The decomposition temperature (T_d = 5 wt% loss) for **TPI-InCz** was 507 °C, **PAI-InCz** was 526 °C, and **CN-PAI-InCz** was 504 °C. **TPI-InCz** has a glass transition temperature (T_g) at 185 °C and a melting temperature (T_m) at 378 °C. **PAI-InCz** exhibits a T_g of 225 °C and a Tm of 450 °C, while **CN-PAI-InCz** shows a T_g of 231 °C and a T_m of 450 °C. (Fig. S6†) **TPI-InCz** had a lower T_m compared to the other two materials, which can be attributed to the presence of diphenyl groups in **TPI-InCz**, effectively suppressing intermolecular interactions. In contrast, **PAI-InCz**, with its high rigidity due to the fused ring structure, exhibited a unique crystallization temperature (T_c) at 327 °C. The exceptional thermal stability of **PAI-InCz** is noteworthy, given its capability to endure the joule heating produced during the operation of OLED devices, thereby ensuring stable and reliable performance.[32]

Electroluminescence (EL) properties

The newly synthesized three materials were used as the emitting layer (EML) in the fabrication of non-doped devices with the following structure: ITO/1,4,5,8,9,11-hexaazatriphenylenehexacarbonitrile (HAT-CN) (5 nm)/*N*,*N*′-di(1-naphthyl)-*N*,*N*′-diphenyl-(1,1′-biphenyl)-4,4′-diamine (NPB) (40 nm)/tris(4-carbazoyl-9-ylphenyl)amine (TCTA) (10 nm)/EML (30 nm)/1,3,5-tris(3-pyridyl-3-phenyl)benzene (TmPyPb) (30 nm)/LiF (1 nm)/Al (200 nm). In this device, HAT-CN was employed as the hole-injection layer, NPB served as the hole-transporting layer, TCTA acted as the exciton blocking layer (EBL), TmPyPb functioned as both the electron-transporting layer (ETL) and the hole-blocking layer (HBL), and LiF and Al were used as the electron-injecting material and the cathode, respectively. The fabricated devices exhibited a low turn-on voltage, ranging approximately from 3.0 to 3.6 V at 1 cd m^{-2}. In terms of device performance, TPA-InCz showed the lowest efficiency with a current efficiency (CE) of 0.54 cd A^{-1}, power efficiency (PE) of 0.30 lm W^{-1}, and EQE of 1.64%. **PAI-InCz**, on the other hand, demonstrated better performance with a CE of 1.44 cd A^{-1}, PE of 1.09 lm W^{-1}, and EQE of 2.62%. The highest efficiency was achieved by **CN-PAI-InCz**, which exhibited a CE of 2.91 cd A^{-1}, PE of 1.93 lm W^{-1}, and EQE of 3.31% (Table 3 and Fig. 6). Also, the maximum luminance of the fabricated **TPI-InCz**, **PAI-InCz**, and **CN-PAI-InCz** devices was measured at 156, 453, and 1178 cm m^{-2} (@ 8 V), respectively.

To further investigate the factors affecting EQE, particularly the carrier recombination efficiency, hole-only devices (HOD)

Table 3 EL performances of non-doped OLED devices at 10 mA cm^{-2}

	V_{on}[a] (V)	CE (cd A^{-1})	PE (lm W^{-1})	EQE (%)	CIE (x, y)	EL_{max} (nm)	Hole mobility (cm^2 V^{-1} s^{-1})	Electron mobility (cm^2 V^{-1} s^{-1})
TPI-InCz	3.61	0.54	0.30	1.64	(0.162, 0.048)	423	5.74×10^{-5}	5.04×10^{-10}
PAI-InCz	3.01	1.44	1.09	2.62	(0.161, 0.067)	431	1.50×10^{-3}	8.82×10^{-10}
CN-PAI-InCz	3.31	2.91	1.93	3.31	(0.155, 0.099)	446	2.66×10^{-4}	1.66×10^{-9}

[a] Turn-on voltage at 1 cd m^{-2}.

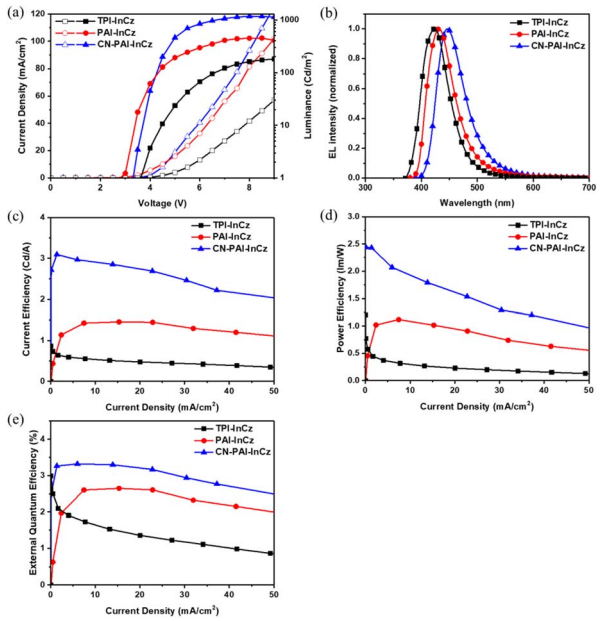

Fig. 6 EL performance of non-doped OLED devices (a) current density (*J*)–voltage (*V*)–luminance (*L*) characteristics, (b) normalized EL spectra, (c) CE–*J* curves, (d) PE–*J* curves, (e) EQE–*J* curves.

and electron-only devices (EOD) were fabricated. The device structures were as follows. The structure of HOD is ITO/TmPyPb (40 nm)/EML (50 nm)/TmPyPb (40 nm)/LiF (1 nm)/Al (100 nm). The structure of EOD is ITO/molybdenum trioxide (MoO_3) (1 nm)/EML (50 nm)/MoO_3 (10 nm)/Al (100 nm).

In these devices, the hole mobility was observed in the order of **TPI-InCz** (5.74×10^{-5} cm^2 V^{-1} s^{-1}) < **CN-PAI-InCz** (2.66×10^{-4} cm^2 V^{-1} s^{-1}) < **PAI-InCz** (1.50×10^{-3} cm^2 V^{-1} s^{-1}). (Fig. S7†) Among the three synthesized materials, **PAI-InCz** exhibited the highest hole mobility. This can be attributed to the composition of **PAI-InCz**, which combines the excellent hole-conducting InCz with the weak acceptor PAI moiety, as well as its high rigidity and planarity, which facilitate efficient hole transport. On the other hand, the electron mobility was lower for all three materials, with **CN-PAI-InCz** having the highest electron mobility (1.66×10^{-9} cm^2 V^{-1} s^{-1}), followed by **PAI-InCz** (8.82×10^{-10} cm^2 V^{-1} s^{-1}) and **TPI-InCz** (5.04×10^{-10} cm^2 V^{-1} s^{-1}). Due to these differences in charge mobility, **TPI-InCz** exhibited the lowest PLQY and poor efficiency, while **PAI-InCz** had the highest PLQY but a mismatched charge balance. In contrast, **CN-PAI-InCz** exhibited the best charge balance, and its deep LUMO energy level due to the introduced CN group facilitated efficient electron injection, resulting in the highest efficiency.[33–35]. (Fig. S8†) Overall, the three materials exhibited significant differences in both hole and electron mobility. While ideal bipolar materials are characterized by similar hole and electron mobility,[36] substantial differences can sometimes be observed due to the abilities of the donor and acceptor constituting the molecule, as well as the symmetry based on the arrangement within the molecule.[37,38] In this study, we not only confirmed shifts in PL wavelength according to the dielectric constant of the solvent through the previously mentioned solvatochromism, but also identified the basis for bipolar molecules by observing results from molecular calculations, which revealed the separation of electron density at HOMO and LUMO levels.

As a result, the order of charge balance aligns with the EQE efficiency trend. The electroluminescence maximum (EL_{max}) peaks of the fabricated devices using **TPI-InCz**, **PAI-InCz**, and **CN-PAI-InCz** were observed at 423 nm, 431 nm, and 446 nm, respectively, consistent with the PL maximum wavelengths. The Commission Internationale de l'Eclairage (CIE) coordinates for these materials were (0.162, 0.048), (0.0161, 0.067), and (0.155, 0.099), all the blue region, particularly **TPI-InCz** and **PAI-InCz**, which exhibited deep-blue emission, making them promising candidates for applications in the TV industry (Fig. S9†).[39] **PAI-InCz** and **CN-PAI-InCz** exhibited similar EL_{max} and PL_{max} values, while **TPI-InCz** showed a discrepancy between EL_{max} and PL_{max}. This is presumed to be due to the slow hole mobility in **TPI-InCz** and the fundamental difference in the luminescence mechanisms between EL and PL. PL involves luminescence generated as excited electrons, caused by an external light source, return to the ground state, whereas EL results from the recombination of electrons and holes injected by an outside electrode source. Additionally, EL is influenced by the recombination site within the EML, which is affected by the mobility of other layers used in the fabricated device. Consequently, improvements can be achieved by utilizing different types of HTL or ETL. Through this research, we have developed a new deep blue material using InCz; however, it exhibited relatively lower device efficiency compared to the commercialized device. The purpose of this study is to present new derivatives demonstrating the capability of introducing various N-type moieties at two nitrogen positions of InCZ. This could be an approach to the synthesis of new derivatives, indicating the potential to create numerous InCz derivatives using diverse substituents, which may lead to improved efficiency. Moreover, enhancing efficiency could be achieved by replacing the HTL and ETL layers in devices or by fabricating doped devices utilizing the synthesized materials as dopants. We plan to delve deeper into these aspects in our future research.

Conclusions

The three newly synthesized blue materials were developed by introducing TPI, PAI, and CN-PAI, all possessing excellent hole characteristics, to the electron-accepting InCz. **TPI-InCz** and **PAI-InCz** exhibited PL maxima in the deep blue region at 410 nm and 431 nm, while **CN-PAI-InCz** emitted light in the real blue region at 452 nm. **CN-PAI-InCz** showed the relatively strong bipolar characteristics among three compounds, as confirmed through solvatochromism experiments and the fabrication of HOD and EOD, demonstrating superior charge balance. When used as the EML in non-doped devices, **CN-PAI-InCz** achieved the highest efficiency with a CE of 2.91 cd A^{-1}, PE of 1.93 lm W^{-1}, and EQE of 3.31%. **PAI-InCz**, characterized by its planarity and high rigidity, exhibited rapid hole mobility, suggesting its potential for use as a HTL. In the fabricated devices, **TPI-InCz**, **PAI-InCz**, and **CN-PAI-InCz** all exhibited electroluminescence in

the blue region, as indicated by their CIE coordinates of (0.162, 0.048), (0.161, 0.067), and (0.155, 0.099), respectively. These materials, characterized by their high rigidity, hold promise for future use as blue OLED materials for TVs. With further improvement through the selection of various carrier materials to enhance charge balance and the development of dopant systems, these materials could play a role in the development of blue OLED technologies.

Author contributions

Conceptualization, G. M. and J. P.; methodology, H. L. and K. L.; validation, K. L.; investigation, G. M., H. K., S. P. (Sangwook Park), and S. P (Sunwoo Park).; writing – original draft preparation, H. L. and J. P.; writing – review and editing, H. L. and J. P.; visualization, H. K.; supervision, J. P.; project administration, J. P.; funding acquisition, J. P.

Conflicts of interest

There are no conflicts to declare.

Acknowledgements

This research was supported by the Basic Science Research Program through the National Research Foundation of Korea (NRF) funded by the Ministry of Education (2020R1A6A1A03048004). This work was partly supported by the GRRC program of Gyeonggi province [(GRRCKYUNGHEE2023-B01), development of ultra-fine process materials based on the sub-nanometer class for the next-generation semiconductors]. This research was supported by Basic Science Research Capacity Enhancement Project through Korea Basic Science Institute (National research Facilities and Equipment Center) grant funded by the Ministry of Education. (No. 2019R1A6C1010052). This work was supported by the Technology Innovation Program (20017832, development of TiN-based electrode materials and ALD equipment for 10 nm DRAM capacitor electrode deposition process) funded By the Ministry of Trade, Industry & Energy (MOTIE, Korea).

References

1 H. Uoyama, K. Goushi, K. Shizu, H. Nomura and C. Adachi, *Nature*, 2012, **492**, 234–238.
2 T. Hatakeyama, K. Shiren, K. Nakajima, S. Nomura, S. Nakatsuka, K. Kinoshita, J. Ni, Y. Ono and T. Ikuta, *Adv. Mater.*, 2016, **28**, 2777–2781.
3 T. Janosik, A. Rannug, U. Rannug, N. Wahlström, J. Slätt and J. Bergman, *Chem. Rev.*, 2018, **118**(18), 9058–9128.
4 M. Cai, M. Auffray, D. Zhang, Y. Zhang, R. Nagata, Z. Lin, X. Tang, C. Y. Chan, Y. Lee, T. Huang, X. Song, Y. Tsuchiya, C. Adachi and L. Duan, *Chem. Eng. J.*, 2021, **420**, 127591.
5 D. J. Shin, S. J. Hwang, J. Lim, C. Y. Jeon, J. Y. Lee and J. H. Kwon, *Chem. Eng. J.*, 2022, **446**, 137181.
6 J. Lee, U. Jo and J. Y. Lee, *ACS Appl. Mater. Interfaces*, 2023, **15**, 21261–21269.
7 F. Huang, X.-C. Fan, Y.-C. Cheng, H. Wu, X. Xiong, J. Yu, K. Wang and X.-H. Zhang, *Angew. Chem., Int. Ed.*, 2023, **62**, e202306413.
8 S. Oda, B. Kawakami, M. Horiuchi, Y. Yamasaki, R. Kawasumi and T. Hatakeyama, *Adv. Sci.*, 2022, **10**, 2205070.
9 D. Kasemann, R. Brückner, H. Fröb and K. Leo, *Phys. Rev. B: Condens. Matter Mater. Phys.*, 2011, **84**, 115208.
10 C. Yin, Y. Zhang, Ti. Huang, Z. Liu, L. Duan and D. Zhang, *Sci. Adv.*, 2022, **8**, eabp9203.
11 Y.-M. Chen, W.-Y. Hung, H.-W. You, A. Chaskar, H.-C. Ting, H.-F. Chen, K.-T. Wong and Y.-H. Liua, *J. Mater. Chem.*, 2011, **21**, 14971–14978.
12 K. M. Youn, H. Lee, H. J. Yoo, Y. H. Jung, J. D. Park, H. Jeong, J. Lee, J. Y. Lee and J. H. Kwon, *J. Mater. Chem. C*, 2020, **8**, 13811–13818.
13 W.-C. Lin, W.-C. Huang, M.-H. Huang, C.-C. Fan, H.-W. Lin, L.-Y. Chen, Y.-W. Liu, J.-S. Lin, T.-C. Chao and M.-R. Tseng, *J. Mater. Chem. C*, 2013, **1**, 6835–6841.
14 Y. Huang, J. Xing, Q. Gong, L.-C. Chen, G. Liu, C. Yao, Z. Wang, H.-Li. Zhang, Z. Chen and Q. Zhang, *Nat. Commun.*, 2019, **10**, 169.
15 X. Tang, L.-S. Cui, H.-C. Li, A. J. Gillett, F. Auras, Y.-K. Qu, C. Zhong, S. T. E. Jones, Z.-Q. Jiang, R. H. Friend and L.-S. Liao, *Nat. Mater.*, 2020, **19**, 1332–1338.
16 Y. Liu, C. Li, Z. Ren, S. Yan and M. R. Bryce, *Nat. Rev. Mater.*, 2018, **3**, 18020.
17 D. Zhang, X. Song, M. Cai, H. Kaji and L. Duan, *Adv. Mater.*, 2018, **30**, 1705406.
18 X. Song, D. Zhang, Y. Lu, C. Yin and L. Duan, *Adv. Mater.*, 2019, **31**, 1901923.
19 X. Zheng, F. Cao, C. Wang, T. Tsuboi, Y. Zhu, Q. Ai, C. Deng, D. Wang, L. Su, Z. Liu and Q. Zhang, *J. Mater. Chem. C*, 2020, **8**, 10021–10030.
20 H. J. Lee, H. L. Lee, S. H. Han and J. Y. Lee, *Chem. Eng. J.*, 2022, **427**, 130988.
21 C.-C. Lai, M.-J. Huang, H.-H. Chou, C.-Y. Liao, P. Rajamalli and C.-H. Cheng, *Adv. Funct. Mater.*, 2015, **25**, 5548–5556.
22 R. K. Konidena, K. R. J. Thomas, D. K. Dubey, S. Sahoo and J.-H. Jou, *Chem. Commun.*, 2017, **53**, 11802–11805.
23 X. Tian, J. Sheng, S. Zhang, S. Xiao, Y. Gao, H. Liu and B. Yang, *Molecules*, 2021, **26**(15), 4560.
24 J. Wang, J. Zhang, C. Jiang, C. Yao and X. Xi, *ACS Appl. Mater. Interfaces*, 2021, **13**(48), 57713–57724.
25 P. Rajamalli, D. Chen, S. M. Suresh, Y. Tsuchiya, C. Adachi and E. Z. Colman, *Eur. J. Org Chem.*, 2021, **2021**(16), 2285–2293.
26 F. Neese, F. Wennmohs, U. Becker and C. Riplinger, *J. Chem. Phys.*, 2020, **152**, 224108.
27 J. T. Buck, R. W. Wilson and T. Mani, *J. Phys. Chem. Lett.*, 2019, **10**(11), 3080–3086.
28 P. Zhang, J. Zeng, J. Guo, S. Zhen, B. Xiao, Z. Wang, Z. Zhao and B. Z. Tang, *Front. Chem.*, 2019, **7**, 199.

29 T. H. Kwon, S. O. Jeon, M. Numata, H. Lee, Y. S. Chung, J. S. Kim, S.-G. Ihn, M. Sim, S. Kim and B. M. Kim, *Nanomaterials*, 2019, **9**(12), 1735.
30 R. Ansari, W. Shao, S.-J. Yoon, J. Kim and J. Kieffer, *ACS Appl. Mater. Interfaces*, 2021, **13**(24), 28529–28537.
31 A. Casey, S. D. Dimitrov, P. S. Tuladhar, Z. Fei, M. Nguyen, Y. Han, T. D. Anthopoulos, J. R. Durrant and M. Heeney, *Chem. Mater.*, 2016, **28**(14), 5110–5120.
32 K. Kwak, K. Cho and S. Kim, *Opt. Express*, 2013, **21**(24), 29558–29566.
33 S. Kang, J.-S. Huh, J.-J. Kim and J. Park, *J. Mater. Chem. C*, 2020, **8**, 11168–11176.
34 W.-Y. Hung, P.-Y. Chiang, S.-W. Lin, W.-C. Tang, Y.-T. Chen, S.-H. Liu, P.-T. Chou, Y.-T. Hung and K.-T. Wong, *ACS Appl. Mater. Interfaces*, 2016, **8**(7), 4811–4818.
35 C. Han, F. Zhao, Z. Zhang, L. Zhu, H. Xu, J. Li, D. Ma and P. Yan, *Chem. Mater.*, 2013, **25**, 4966–4976.
36 D. W. Lee, J. Hwang, H. J. Kim, H. Lee, J. M. Ha, H. Y. Woo, S. Park, M. J. Cho and D. H. Choi, *ACS Appl. Mater. Interfaces*, 2021, **13**, 49076–49084.
37 C.-H. Chiu, N. R. A. Amin, J.-X. Xie, C.-C. Lee, D. Luo, S. Biring, K. Sutanto, S.-W. Liu and C.-H. Chen, *J. Mater. Chem. C*, 2022, **10**, 4955–4964.
38 C. Cao, W.-C. Chen, S. Tian, J.-X. Chen, Z.-Y. Wang, X.-H. Zheng, C.-W. Ding, J.-H. Li, J.-J. Zhu, Z.-L. Zhu, Q.-X. Tong and C.-S. Lee, *Mater. Chem. Front.*, 2019, **3**, 1071–1079.
39 D. Yu, F. Zhao, Z. Zhang, C. Han, H. Xu, J. Li, D. Ma and P. Yan, *Chem. Commun.*, 2012, **48**, 6157–6159.